symmetry

MDPI

Article

Persistent Homology Analysis for Dense QCD Effective Model with Heavy Quarks

Kouji Kashiwa [1,*], Takehiro Hirakida [2] and Hiroaki Kouno [3]

[1] Department of Computer Science and Engineering, Fukuoka Institute of Technology, Fukuoka 811-0295, Japan
[2] Izumi Chuo High School, Izumi 899-0213, Japan
[3] Department of Physics, Saga University, Saga 840-8502, Japan
* Correspondence: kashiwa@fit.ac.jp

Abstract: The isospin chemical potential region is known as the sign-problem-free region of quantum chromodynamics (QCD). In this paper, we introduce the isospin chemical potential to the three-dimensional three-state Potts model to mimic dense QCD; e.g., the QCD effective model with heavy quarks at finite density. We call it the QCD-like Potts model. The QCD-like Potts model does not have a sign problem, but we expect it to share some properties with QCD. Since we can obtain the non-approximated Potts spin configuration at finite isospin chemical potential, where the simple Metropolis algorithm can work, we perform the persistent homology analysis toward exploring the dense spatial structure of QCD. We show that the averaged birth-death ratio has the same information with the Polyakov loop, but the maximum birth-death ratio has additional information near the phase transition where the birth-death ratio means the ratio of the creation time of a hole and its vanishing time based on the persistent homology.

Keywords: QCD-like Potts model; persistent homology; confinement–deconfinement transition

Citation: Kashiwa, K.; Hirakida, T.; Kouno, H. Persistent Homology Analysis for Dense QCD Effective Model with Heavy Quarks. *Symmetry* **2022**, *14*, 1783. https://doi.org/10.3390/sym14091783

Academic Editor: Maxim Yu. Khlopov

Received: 5 August 2022
Accepted: 22 August 2022
Published: 26 August 2022

1. Introduction

Elucidating the phase structure of Quantum Chromodynamics (QCD) at finite temperature (T) and real chemical potential ($\mu_{\rm R}$) is an interesting and important subject for elementary, nuclear, and hadron physics. Unfortunately, there is the sign problem in QCD at finite $\mu_{\rm R}$, and thus, we cannot have a reliable QCD phase diagram yet; for example, see [1] for details of the sign problem. Several approaches have been proposed so far to tackle the sign problem, but the sign problem is not resolved satisfactorily in QCD at present.

To avoid the sign problem, one possibility is to employ the QCD effective models. Since the sign problem is strongly related to the correlation between the gauge field and the chemical potential in the Dirac operator, simplifications of the gauge field dynamics sometimes weaken the sign problem. For example, the simplest Nambu–Jona-Lasinio (NJL) model [2] does not have the sign problem at finite density. Of course, such simplification loses some properties of QCD, but we can learn several important lessons from the models. It should be noted that the sign problem can still remain even if we simplify the gluon dynamics; it depends on how much original nature of QCD is restored.

The Potts model with a properly constructed external field is the well-known QCD effective model with heavy quarks; for example, see [3] for details of the Potts model. The external field consists of the quark mass and the chemical potential, and thus, there is a sign problem at finite $\mu_{\rm R}$ even if it is weaker than the original QCD. There are several attempts to avoid and/or weaken the sign problem appearing in the Potts model [4,5].

There is the analytic expectation that there is a crystalline structure in a certain parameter region in the low-dimensional Potts model with the external field via the transfer matrix approach; see [6] and references therein. However, the existence of such a non-trivial spatial structure is not yet confirmed in the higher-dimensional system [7]. The Potts model

can be regarded as the QCD effective model with heavy quarks, and thus, we may expect a non-trivial spatial structure even in QCD if it exists. In this paper, we try to sidestep the sign problem and investigate the possibility of non-trivial spatial structure from the topological viewpoint.

There are some approaches to weaken the sign problem in QCD and in some other theories/models at moderate $\mu_{\rm R}$ with low T. Famous examples are the complexification of dynamical variables such as the comlpex Langevin dynamics [8,9], the Lefshcetz thimble method [10,11], and the path optimization method [12,13] . In addition, we can discuss the region using the canonical approach [14–21], partially. However, those methods are not perfect yet, and therefore, it is difficult to apply those methods in the whole $\mu_{\rm R}$ region.

In this study, we introduce the isospin chemical potential ($\mu_{\rm iso}$) to the Potts model and investigate its spatial structure to mimic the dense QCD system with heavy quarks. The important point is that it is known that the $\mu_{\rm R}$ region and the $\mu_{\rm iso}$ region are equivalent in the region where pion condensation does not appear at least in the large $N_{\rm c}$ limit where $N_{\rm c}$ means the number of colors; see [22] as an example. This indicates that we can approximately investigate the $\mu_{\rm R}$ region via the $\mu_{\rm iso}$ region in the model. Since we can resolve the sign problem in the Potts model at a finite $\mu_{\rm iso}$, we perform the persistent homology analysis [23,24].

The persistent homology analysis has been applied to the QCD effective model, e.g., the effective Polyakov-line model [25], and it is expected to be useful to investigate the spatial structure such as the center cluster structure; see [26–28] for details of the center cluster. In this study, we investigate the question of whether there is a non-trivial spatial structure or not at finite density via the QCD-like Potts model. This study is a first step in investigating the spatial structure of QCD at finite density with persistent homology. Actually, there are several studies which use the persistent homology to investigate the phase transition [29–34]. In these papers, the authors try to detect and investigate phase transition appearing in the condensed matter system by using the persistent homology. In addition, there are some other applications in several research fields, such as the string landscape and the structure of the universe [35,36]. We work in the same direction as [29–32].

This paper is organized as follows. In the next Section 2, we show the formalism of the Potts model with the isospin chemical potential. In addition, we briefly explain the persistent homology analysis. Section 3 shows our numerical results and Section 4 is devoted to the summary.

2. Formalism

In this paper, we employ the three-dimensional three-state Potts model with the external field as the QCD effective model with heavy quarks; see [37–39] for details of the relation between the Potts model and QCD. Here, we summarize the Potts model and its extension to include the isospin chemical potential. Some problems for the Potts model with the complexification of dynamical variables are discussed in Appendix A.

2.1. QCD-like Potts Model

In this subsection, we summarize theoretical insights into the Potts model and its extension.

2.1.1. Standard Potts Model with External Field

The Potts-model energy with the external field is given by

$$E = -\kappa \sum_{\mathbf{x},\mathbf{i}} \delta_{k_{\mathbf{x}} k_{\mathbf{x}+\mathbf{i}}} - h \sum_{\mathbf{x}} k_{\mathbf{x}}, \tag{1}$$

where $\mathbf{i}$ means the unit vector in the three-dimensional space, κ denotes the coupling constant, h is the external magnetic field, and $k_{\mathbf{x}}$ are $\mathbb{Z}_Q$ values which take $0, 1, \cdots, Q-1$ at site $\mathbf{x}$. This model is the so-called Q-state Potts model. In this study, we impose the periodic boundary condition for Potts spins.

If κ is positive, the first term in Equation (1) makes spins align to the same direction. In the case with negative κ, nearest-neighbor spins favor the different direction. The last term explicitly breaks the $\mathbb{Z}_Q$ symmetry of the system.

2.1.2. Map of Chemical Potential to External Field

To make the Potts model relate to QCD, we here consider following extension of the Potts energy based on [37];

$$E = -\kappa \sum_{\mathbf{x},\mathbf{i}} \delta_{\Phi_{\mathbf{x}}\Phi_{\mathbf{x}+\mathbf{i}}} - N_{\mathrm{f}} \sum_{\mathbf{x}} \left(h_+ \Phi_{\mathbf{x}} + h_- \bar{\Phi}_{\mathbf{x}} \right), \tag{2}$$

where N_{f} denotes the number of flavors where we assume that all the flavors are degenerate, $h_\pm$ is the external field explained in Equation (3), and $\Phi_{\mathbf{x}}$ ($\bar{\Phi}_{\mathbf{x}}$) means the $\mathbb{Z}_3$ values (its conjugate) at each site shown in Equation (4); it corresponds to the Polyakov loop in QCD where the number of colors is set to 3. The color structure is encoded in the functional form of Φ and $\bar{\Phi}$. For N_{f}, we set it to 2 in all the calculations in this paper. Since Potts spins are defined on the lattice, we put the space index $\mathbf{x}$ as the subscript of Φ unlike the QCD case (A1). The relations between the Potts model and QCD are clearly shown in [37–39]. This model is sometimes referred to as the three-dimensional $\mathbb{Z}_3$ spin model [7].

The external fields consist of the quark mass and the chemical potential as

$$h_\pm = e^{-\beta(M \mp \mu_{\mathrm{R}})}, \tag{3}$$

which is induced from the fermion determinant in the QCD partition function; see Appendix in [39] for details. If the quark mass is sufficiently large in QCD, the three-dimensional three-state Potts model with the external field can be treated as the effective model of QCD at finite T and μ_{R}.

In this study, the Potts spin at the site $\mathbf{x}$ is taken to be $k_{\mathbf{x}} = 0, 1, 2$, and then, the Polyakov loop and its conjugate are defined as

$$\Phi_{\mathbf{x}} = e^{i2\pi k_{\mathbf{x}}/3}, \quad \bar{\Phi}_{\mathbf{x}} = e^{-i2\pi k_{\mathbf{x}}/3}. \tag{4}$$

Therefore, the spatial averaged values are defined as

$$\Phi = \frac{1}{V} \sum_{\mathbf{x}} \Phi_{\mathbf{x}}, \quad \bar{\Phi} = \frac{1}{V} \sum_{\mathbf{x}} \bar{\Phi}_{\mathbf{x}}, \tag{5}$$

where V is the spatial volume of the lattice system, $V = L^3$. It should be noted that this functional form (4) is just valid in the Potts model: we can easily understand that the Polyakov loop in the Potts model mimics the Polyakov loop in QCD by using the setting $\theta_3 = 0$ and $\theta_8 = 2\pi k/3$ with $k = 0, 1, 2$ from Equations (A1)–(A3). Therefore, the Potts model qualitatively captures the behavior of the Polyakov loop in QCD by using certain values of θ_8; $\theta_8 = 2\pi k_{\mathbf{x}}/3$.

2.1.3. Extension to Isospin Chemical Potential

One possibility to obtain the spin configurations at finite density even if those are approximated configurations, the isospin chemical potential (μ_{iso}) is a good candidate; we set $\mu_u = \mu_{\mathrm{R}}$ and $\mu_d = -\mu_{\mathrm{R}}$ in the two-flavor (u, d) system. In this setting, the quark number density is always zero, but the isospin density can be nonzero. In the realistic system, the isospin chemical potential relates to the realistic up and down quarks, but here, we consider the system with two-kind of heavy quarks and these heavy quarks are degenerated. Thus, the present isospin chemical potential just indicates the asymmetry of heavy quarks. We will discuss the realistic isospin chemical potential elsewhere with a more suitable model.

If the pion and diquark condensates appear, the system with $\mu_{\rm iso}$ shows the difference with that with $\mu_{\rm R}$, but the systems share similar properties when they do not appear in the systems. In this paper, we are interested in the system with the heavy quarks, and thus, both condensations can be neglected. Therefore, we here employ the system with $\mu_{\rm iso}$ to investigate the spatial structure of the spin configuration of Potts model at finite density. The Potts energy with $\mu_{\rm iso}$ is then given by

$$\begin{aligned} E_{\rm iso} &= -\kappa \sum_{\mathbf{x},\mathbf{i}} \delta_{\Phi_{\mathbf{x}}\Phi_{\mathbf{x}+\mathbf{i}}} - \sum_{\mathbf{x}} \Big[(h_+ \Phi_{\mathbf{x}} + h_- \bar{\Phi}_{\mathbf{x}}) + (h_- \Phi_{\mathbf{x}} + h_+ \bar{\Phi}_{\mathbf{x}}) \Big] \\ &= -\kappa \sum_{\mathbf{x},\mathbf{i}} \delta_{\Phi_{\mathbf{x}}\Phi_{\mathbf{x}+\mathbf{i}}} - \sum_{\mathbf{x}} \Big[h_+ (\Phi_{\mathbf{x}} + \bar{\Phi}_{\mathbf{x}}) + h_- (\Phi_{\mathbf{x}} + \bar{\Phi}_{\mathbf{x}}) \Big] \\ &= -\kappa \sum_{\mathbf{x},\mathbf{i}} \delta_{\Phi_{\mathbf{x}}\Phi_{\mathbf{x}+\mathbf{i}}} - N_{\rm f} \sum_{\mathbf{x}} \Big[(h_+ + h_-) \cos(\Phi_{\mathbf{x}}) \Big] \in \mathbb{R}. \end{aligned} \tag{6}$$

Since the external field term facilitates $k = 0$ for the spin configuration, it mimics the behavior of $\Phi = \bar{\Phi} \to 1$ with $\mu_{\rm R} \to \infty$. Of course, $\Phi = \bar{\Phi} \to 0$ with $\kappa \to 0$ and $\mu_{\rm R} \to 0$ is naturally obtained. Therefore, we have these desirable behaviors from the isospin chemical potential in the Potts model, and these are in sharp contrast with the complexfied Potts model discussed in Appendix A.

In the Potts model, we do not introduce the chiral, diquark, and also the pion condensation, and thus, the $\mu_{\rm R}$ and $\mu_{\rm iso}$ regions are expected to be almost consistent with each other based on the knowledge obtained in the orbifold equivalence; for example, see [22]. This fact indicates that we can approximately obtain the Potts spin configuration with $\mu_{\rm R}$ via the $\mu_{\rm iso}$ region, and then, we can investigate the dense spatial structure, approximately.

2.2. Observables

The most simple quantity that can clarify the system change is the spatially averaged Polyakov loop defined as

$$\langle \Phi \rangle = \Big\langle \frac{1}{V} \sum_{\mathbf{x}} \Phi_{\mathbf{x}} \Big\rangle, \tag{7}$$

where $\langle \cdots \rangle$ means the value averaged by the configuration. This quantity can represent the bulk properties of the system, but it cannot see the non-trivial spatial structure.

To investigate the spatial structure of the system, one possible quantity is the spatial correlator of the Polyakov loop, which may be fitted as

$$\langle \Phi_0 \Phi_r^\dagger \rangle \sim e^{-m_{\rm R} r} \cos(m_{\rm I} r), \tag{8}$$

where Φ_0 means the Polyakov loop at the origin, $m_{\rm R,I}$ can be interpreted as the real and imaginary part of the effective mass of Potts spins and r is the Euclidean distance between two Polyakov-loop operators, $r = \sqrt{x^2 + y^2 + z^2}$. At the critical point, the form of the fitting function is slightly modified. However, the rotational symmetry is explicitly broken by the lattice discretization, and also, since we do not know the actual functional form of the oscillating mode, we consider the correlator for the x-direction in this paper. From the spatial correlator, we can investigate the simple spatial structures of the system such as the periodic spatial oscillation (inhomogeneity); see [40] for the case of the $1+1$ dimensional Gross–Neveu model as an example. Actually, we calculate $\langle f(\Phi_0) f(\Phi_x) \rangle$ where $f(A)$ means Re or Im of A. Unfortunately, these quantities are usually noisy, and thus, we need good statistics.

In addition to the above quantities, we consider the persistent homology to investigate whether there is complicated spatial structure of the system or not. Some details of persistent homology are explained in the next Section 2.3. A good point is that this quantity is less noisy than the spatial correlator since it is directly related with the topological structure of the data.

In the next subsection, we briefly explain the persistent homology, but the procedure is almost the same with that presented in [25].

2.3. Persistent Homology Analysis

In this study, we employ the persistent homology to investigate the spatial structure of the model at finite density: persistent homology is known to clarify non-trivial spatial structures [29,41,42] and also hidden order [30]. In the numerical estimation of persistent homology, we use the homcloud [43]. Since the persistent homology is a complicated mathematical concept, we only show a brief explanation here. If the reader is interested in mathematical details of the persistent homology, see the text and conceptual figures in Section II of [25] and references therein.

2.3.1. Setting of Data Space

In the QCD-like Potts model, there are three independent directions of spin degrees of freedom for each site. Let us consider the datasets A, B, and C; we save the spatial structure for the datasets. For sites with $k = 0$ spin, the corresponding data (coordinate data) are "ON" (occupied) in the dataset A, but other sites in the dataset A are "OFF" (empty) if $k \neq 0$ spins are realized. Via the setting, we can save the spatial structure for $k = 0$ spins into the dataset A. Similarly, we can save the spatial structure for the $k = 1$ and $k = 2$ spins in the datasets B and C, respectively.

In the case of the Polyakov line model analyzed in [25], we need to divide the Polyakov loop into three domains based on the center symmetry and construct the datasets A, B and C. In the QCD-like Potts model, however, we can simply divide the data space into three datasets because the Potts spins are discrete $\mathbb{Z}_3$ quantities by definition.

2.3.2. Birth and Death Times of Holes

After setting the datasets A, B and C, we can consider filtration for each data point, and filtration leads to persistent homology. In persistent homology analysis, we consider the r-ball model. The ball has the radius r for each data point which is corresponding to occupied sites. The center of each ball is set to the position of each site. The value of r is controlled by the fictitious time t. When r is sufficiently small (t is small), each ball is isolated, but the neighborhood balls overlap when r becomes large (t is large). Therefore, there should be a time when the hole appears for the overlapped balls; this time is called the *birth time*, t_B. Of course, such a hole will be vanish when r becomes sufficiently large; this time is the so-called *death time*, t_D. Unfortunately, the construction of r balls is numerically difficult, and thus, we employ the alpha complex to approximate the r-ball model; see [25] for details of the alpha complex as an example. Then, the birth and death times are related to the squared radius of the ball, r^2.

Figure 1 shows the persistent diagram for randomly distributed data as an example. Here, about 33%, 40%, 50%, and 60% of the sites are occupied from the top-left to the right-bottom panel. The situation with occupation 33% corresponds to the ideal confined phase where non-trivial spatial structures are absent, and thus, deviations from the randomly distributed case should be related with the confinement–deconfinement nature and also the spatial non-trivial structure. In the case of the uniform distributed data which means that all sites are occupied, there are only the trivial holes; the actual value of the birth and death times for the trivial holes are $t_{\mathrm{B}} = 0.5$ and $t_{\mathrm{D}} = 0.75$, respectively. Those trivial holes can be easily imaged from the system where all sites are occupied; the system consists of the smallest cubes. This situation corresponds to the ideal deconfined phase for the $k = 0$ spins in this lattice model. The dominant hole structures are clarified in [25] in the confined phase at low κ and zero density.

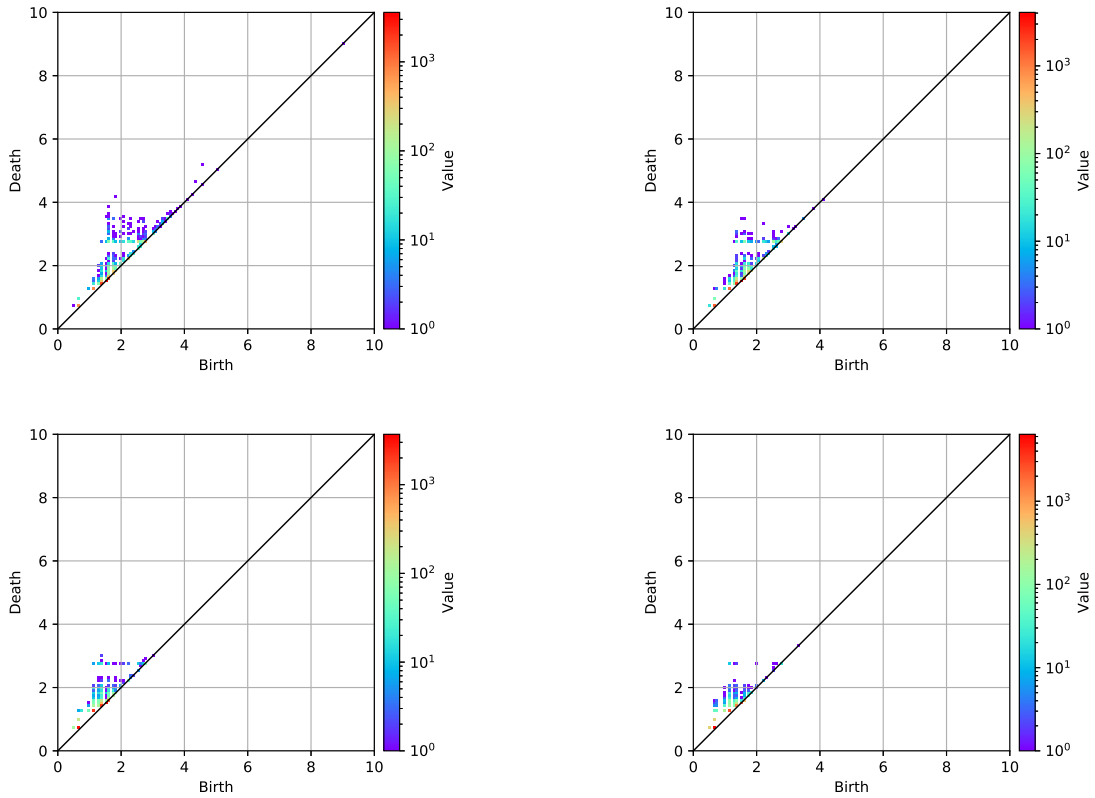

Figure 1. The persistent diagram for randomly distributed data in the 30^3 squared lattice system as a function of the birth and death times. The occupation ratio of the system is about 33%, 40%, 50%, and 60% from the top-left → top-right → left bottom → right-bottom panels, respectively. In the legend, Value means the number of data points which appear at the same point.

2.3.3. Ratio of Birth and Death Times

Since the persistent diagram, which is the two-dimensional diagram, is not convenient in the lattice simulation because we must take the configuration average, the two-dimensional diagram is obtained for each configuration. To simply visualize the persistent diagram, the averaged ratio of birth and death times have been proposed in [25];

$$R = \left\langle \frac{1}{N_h} \sum_i \frac{t_{D,i}}{t_{B,i}} \right\rangle, \tag{9}$$

where N_{h} is the number of all possible holes and $\sum_i$ means that we sum up t_D/t_B for all possible holes. In this study, we show this ratio in addition to the standard persistent diagram.

However, the simple definition of the average ratio (9) may not be good because relatively trivial holes that appear near the diagonal line on the persistent diagram can dominate R; it is known that distant data from the diagonal line usually have meaningful non-trivial spatial structures. Therefore, we will investigate the maximum ratio for all possible holes in Section 3 in addition to the above average ratio. Such a maximum ratio is expected to be relevant for the non-trivial large spatial structure.

3. Numerical Results

In this study, we used the squared $V = L^3 = 30^3$ lattice system. We generate 10^3 configurations for each L^3 update (1 Monte Carlo step) after thermalization using the standard Metropolis algorithm; the transition probability ($\mathcal{P}$) for acceptance or rejection of the single spin flip is defined as $\mathcal{P} = \min[1, \exp(-\beta \Delta E_{\mathrm{iso}})]$ where β is the inverse temperature $\beta = 1/T$ and ΔE_{iso} is the energy difference about the single spin flip. The lattice spacing is set to $a = 1$.

Statistical errors are estimated using the Jackknife method. For the random number generation, we employ the Mersenne Twister algorithm [44]. The mass parameter M and the temperature T are set to 10 and 1 throughout the calculation, respectively.

Figure 2 shows the Monte Carlo evolution of the spatially averaged Polyakov loop. The left-side (right-side) panel is the result with $\kappa = 0.6$ and $\mu_{\rm iso} = 2$ ($\kappa = 0.6$ and $\mu = 6$) after thermalization as a typical example. This figure means that we can generate configurations well even at finite $\mu_{\rm iso}$.

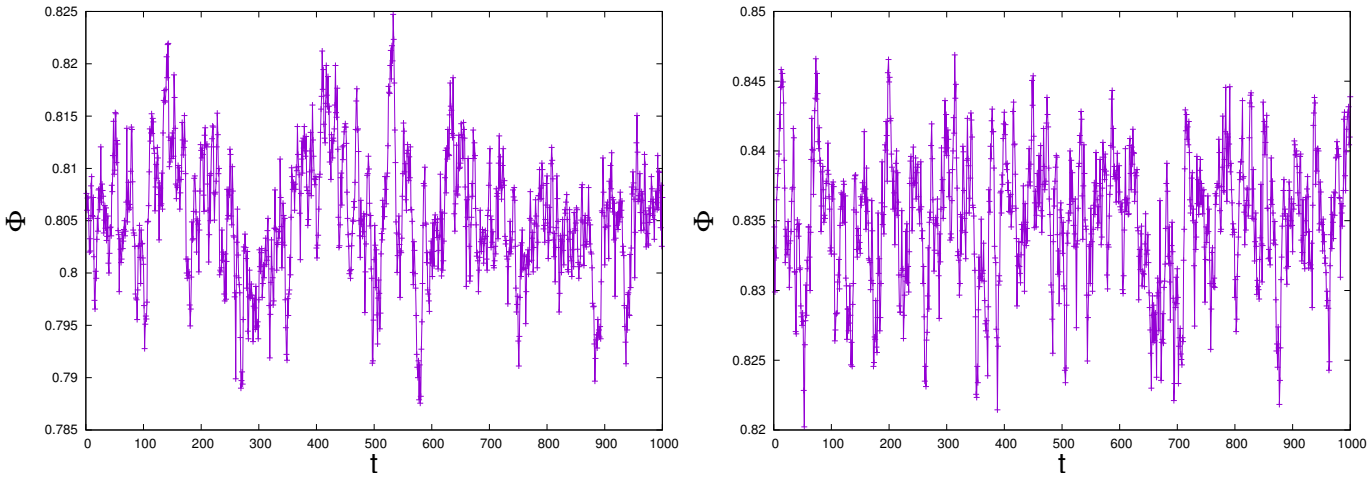

Figure 2. The Monte Carlo evolution of the spatial averaged Polyakov loop after thermalization. The left (right) panel is the result with $\kappa = 0.6$ and $\mu_{\rm iso} = 2$ ($\kappa = 0.6$ and $\mu_{\rm iso} = 6$). Each symbol is the result with corresponding configuration which is obtained via the standard Metropolis algorithm. The horizontal axis t means the label number of configurations.

3.1. Basic Phase Structure

Figure 3 shows the κ-dependence of the Polyakov loop with $\mu_{\rm iso} = 0, 6, 7$, and 8. Statistical errors are small, and therefore, the error bars are in the symbols. Because of the finite-size effect, the phase transitions are smeared if they exist in the thermodynamic limit. In the Potts model, κ is treated as the temperature, and thus, we can see the increasing behavior of $\langle\Phi\rangle$ with increasing κ. In addition, $\langle\Phi\rangle$ increases with increasing $\mu_{\rm iso}$ as we expected: since $\mu_{\rm iso}$ enhances the explicit $\mathbb{Z}_3$ symmetry breaking and it leads nonzero $\langle\Phi\rangle$, the first-order thermal phase transition is weakened when $\mu_{\rm iso}$ becomes large. In the present model, statistical errors are under control for each $\mu_{\rm iso}$. Therefore, we can think that the present QCD-like Potts model shares several properties with thermal and dense QCD matter with heavy quarks, and thus, it is a convenient model in this study. It is noted again that the QCD-like Potts model does not have the sign problem, and thus, we can have exact Potts spin configurations.

Figure 4 shows the mean value of the Polyakov loop in the $\mu_{\rm iso}$-κ plane. Statistical errors estimated using the Jackknife method are quite small, and thus, we do not show them here. We can clearly see the κ- and the $\mu_{\rm iso}$-dependence of $\langle\Phi\rangle$ from the figure, and the behavior is well matched with our expectation in dense QCD with heavy quarks. At low $\mu_{\rm iso}$, there is a first-order thermal transition, but not at large $\mu_{\rm iso}$ because the $\mu_{\rm iso}$-contribution explicitly breaks the $\mathbb{Z}_3$ symmetry as explained above. This indicates that there should be the second-order transition point, which is the critical endpoint at finite κ and $\mu_{\rm iso}$. In the next subsection, we discuss the spatial structure at finite $\mu_{\rm iso}$.

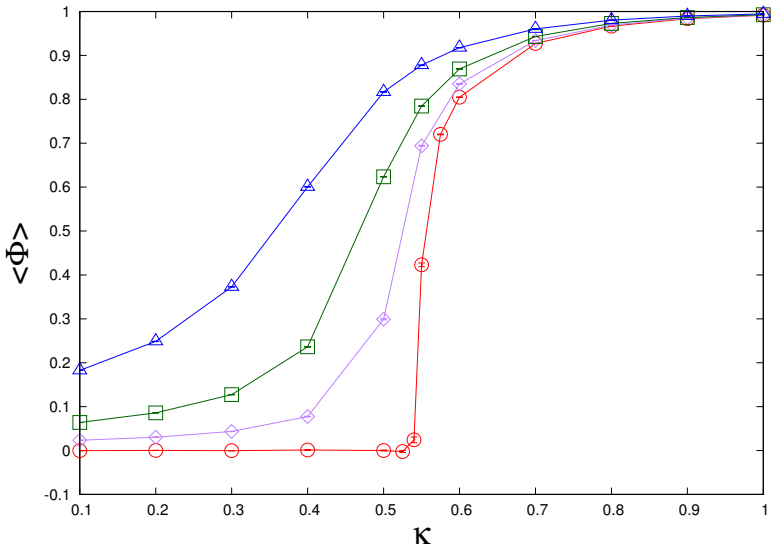

Figure 3. The κ-dependence of the Polyakov loop. The open circle, diamond, square, and triangle symbols are results with $\mu_{\rm iso} = 0, 6, 7$ and 8, respectively. Lines are just eye guides.

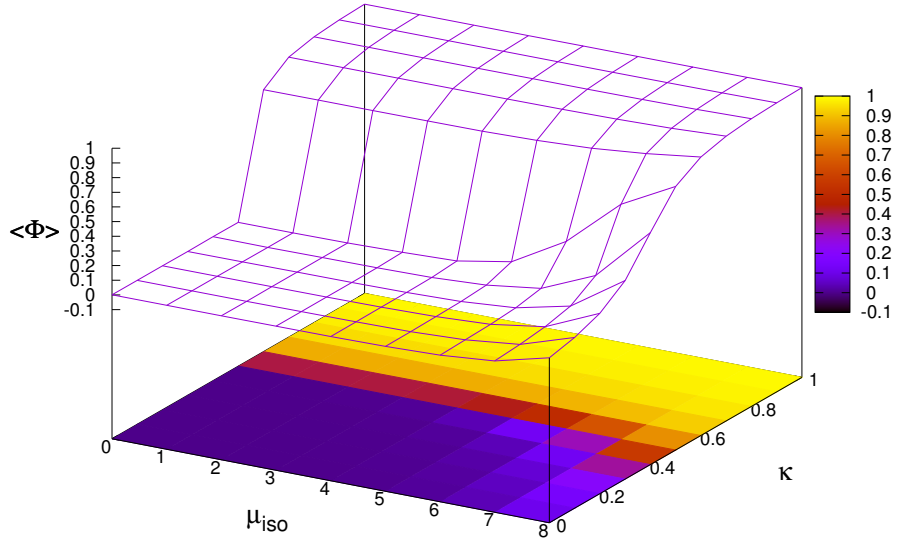

Figure 4. The mean value of Polyakov loop on the $\mu_{\rm iso}$-κ plane. Statistical errors are small, and thus, we do not show them here.

3.2. Spatial Structure

In this section, we investigate the spatial structure at finite $\mu_{\rm iso}$ using spatial correlators and persistent homology. Figure 5 shows the spatial correlators for $\mathrm{Re}\,\Phi$ and $\mathrm{Im}\,\Phi$ at $\mu_{\rm iso} = 5$ with $\kappa = 0.3, 0.4, 0.5$, and 0.6 from the top to the bottom panel. Left (right) panels are result of the spatial correlator for the real (imaginary) part of the Polyakov loop. Since the Polyakov loop is a complex quantity, the correlator must be complex. Therefore, we here show the real and imaginary parts individually. The spatial correlators are very noisy compared to the Polyakov loop with the present statistics. From the figures, we cannot see a clear tendency of the spatial oscillation within the interval 2σ; we may expect the non-trivial structure around $\kappa = 0.5$ if it exists.

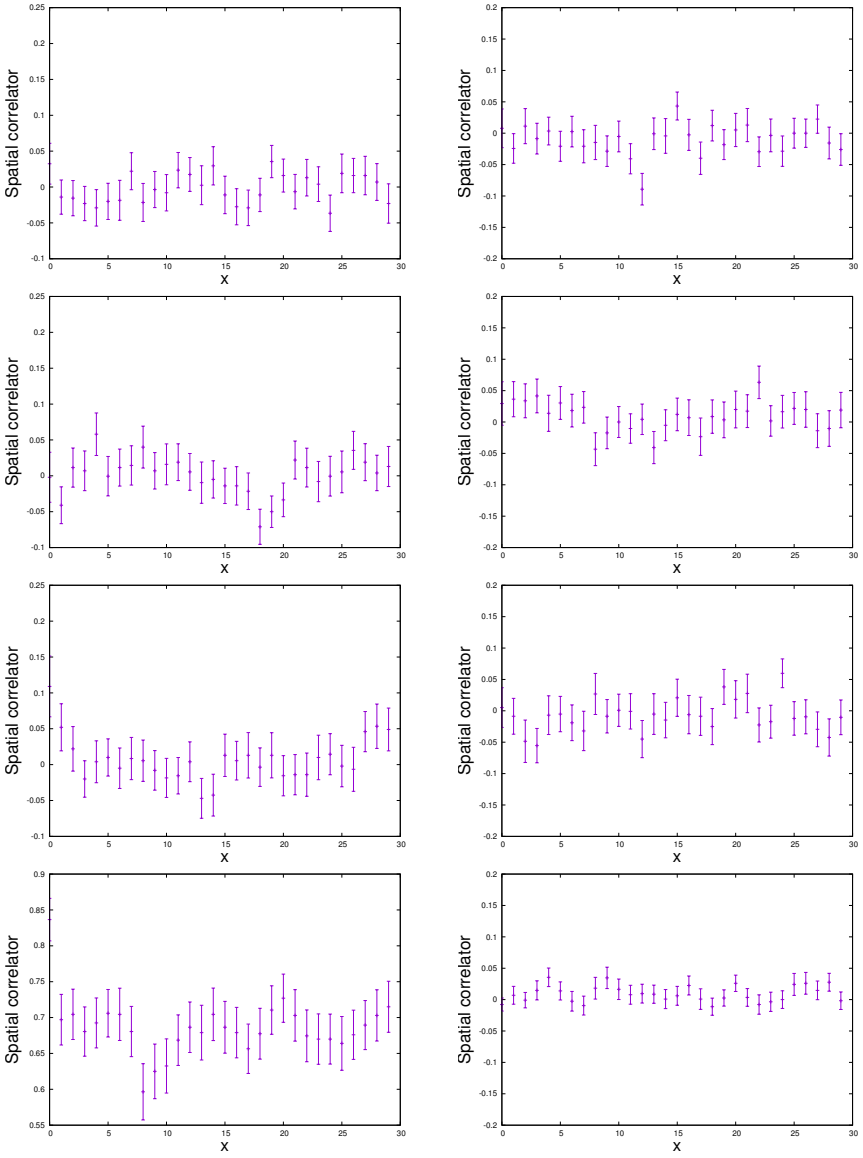

Figure 5. The spatial correlators for the x-direction at $\mu_{\rm iso} = 5$ with $\kappa = 0.3, 0.4, 0.5$, and 0.6 from the top to the bottom panel, respectively. The left and right panels show the spatial correlators for the real and imaginary parts of the Polyakov loop, respectively.

Figure 6 shows persistent diagrams at $\kappa = 0.3, 0.4, 0.5$, and 0.6 with $\mu_{\rm iso} = 0$. The persistent homology analysis then detects the phase transition from sudden change of the persistent diagram. In addition, from the figures, we can see the qualitative difference at intermediate κ. When we compare the results with $\kappa = 0.3$ and 0.6, the distribution appears to simply shrink, but the distribution is temporally enlarged at intermediate κ. This means that possible types of holes are changed, and finally, only trivial cubes persist. This indicates that the system forms the cluster-like structure at intermediate κ because the QCD-like Potts model has the first-order thermal phase transition at $\mu_{\rm iso} = 0$ in the thermodynamic limit.

Figure 7 shows the persistent diagrams at $\kappa = 0.3, 0.4, 0.5$, and 0.6 with $\mu_{\rm iso} = 5$ as an example of the intermediate $\mu_{\rm iso}$ case. From these figures, we can see the similar tendency of Figure 6 at intermediate κ, but we will see that the maximum birth-death ration is not changed so much unlike the result with $\mu_{\rm iso} = 0$; details are discussed later.

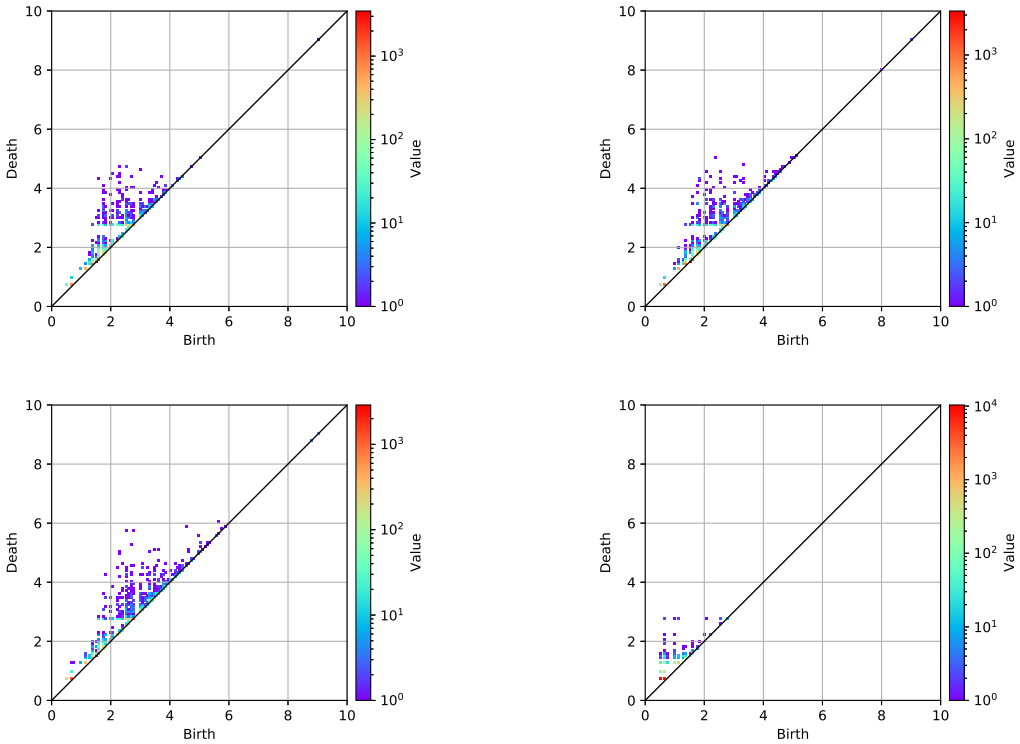

Figure 6. The persistent diagram at $\mu = 0$ for $k = 0$ spins; e.g., the dataset A. Panels are results with $\kappa = 0.3, 0.4, 0.5$, and 0.6 for one particular configuration from the left-top $\rightarrow$ right-top $\rightarrow$ left-bottom $\rightarrow$ the right-bottom panels, respectively.

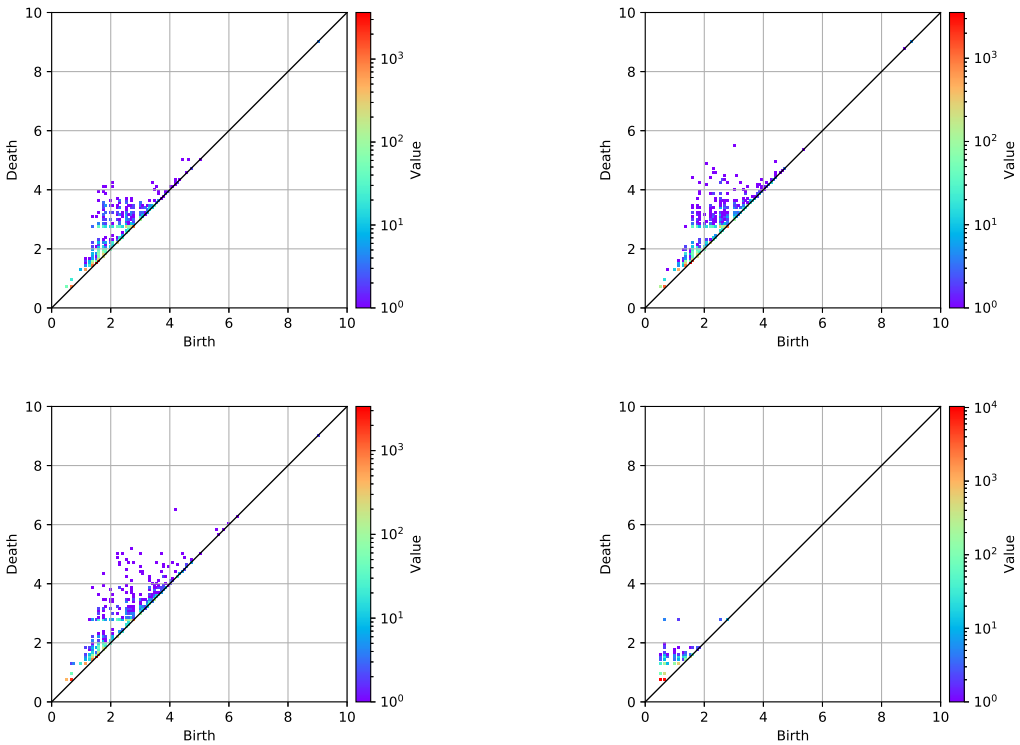

Figure 7. The persistent diagram at $\mu = 5$ for $k = 0$ spins; e.g., the dataset A. Panels are results with $\kappa = 0.3, 0.4, 0.5$, and 0.6 for one particular configuration from the left-top $\rightarrow$ right-top $\rightarrow$ left-bottom $\rightarrow$ right-bottom panels, respectively.

Figure 8 shows the persistent diagrams with $\mu_{\rm iso} = 2, 4, 6$, and 8 with $\kappa = 0.2$. There are no non-trivial changes at finite $\mu_{\rm iso}$. This indicates that there is no first-order phase transition and also no non-trivial spatial structure; we can expect that the crossover is realized along the $\mu_{\rm iso}$ direction at $\kappa = 0.2$. Actually, the chiral symmetry is not present in this model, and thus, there are no mechanisms which enhance the phase transition at low κ. To investigate the persistent homology more deeply, we next consider the averaged ratio and the maximum ratio of the birth and the death time.

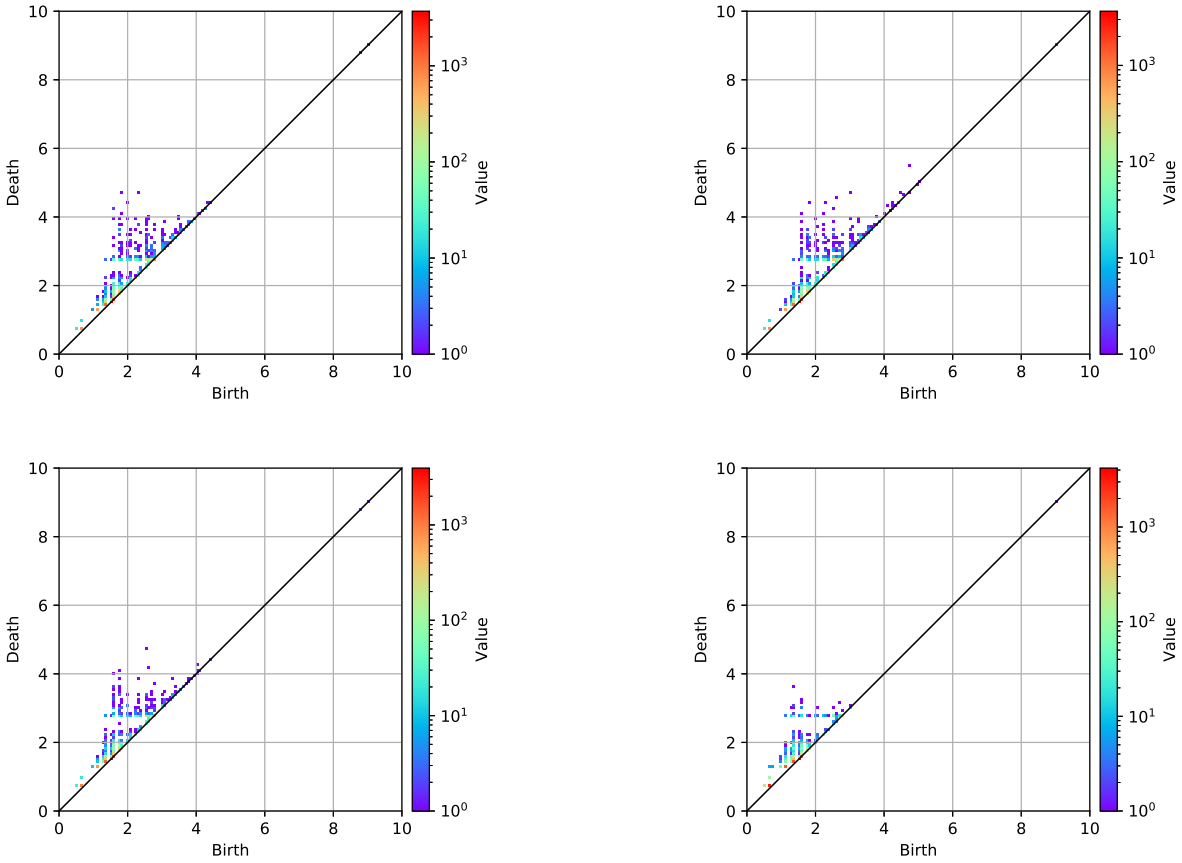

Figure 8. The persistent diagram at $\kappa = 0.2$ for $k = 0$ spins; e.g., the dataset A. Panels are results with $\mu_{\rm iso} = 2, 4, 6$, and 8 for one particular configuration from the left-top $\rightarrow$ right-top $\rightarrow$ left-bottom $\rightarrow$ right-bottom panels, respectively.

The above persistent diagrams are obtained by using one particular configuration, and thus, we show the result of the ratio of birth and death times with the configuration average in Figure 9. Statistical errors are small, and thus, they are hidden in the symbols. The averaged ratio of birth and death times is shown in the top panel of Figure 9; we can expect that the averaged ratio is responsible for the bulk properties of the system. From the upper panel of the figure, we can see the clear tendency of the first-order transition at small $\mu_{\rm iso}$ from the steep change in the averaged ratio. Since the holes which have distinct ratio from the diagonal line on the persistent diagram are responsible for important spatial structures in the persistent homology analysis, we also show the maximum ratio at $\mu_{\rm iso} = 0, 5, 6$ and 7. At low $\mu_{\rm iso}$, the maximum ratio temporally decreases at intermediate κ and it has a peak after its decreasing behavior ends. This indicates that small spatial structures are developed as we approach the first-order transition and after larger spatial structures are formed. Interestingly, we can find the flat region with increasing κ at intermediate $\mu_{\rm iso} \sim 5$. In this region, there is no change of the topological (large spatial) structure of the system and it may indicate the critical endpoint because the enhancement of

the correlation length is expected, and then, the topological structure may not be changed so much; there may be the block-spin transformation invariance for the large spatial structure. This also indicates that there are no non-trivial spatial structures such as the oscillation near the critical endpoint, at least, in this model.

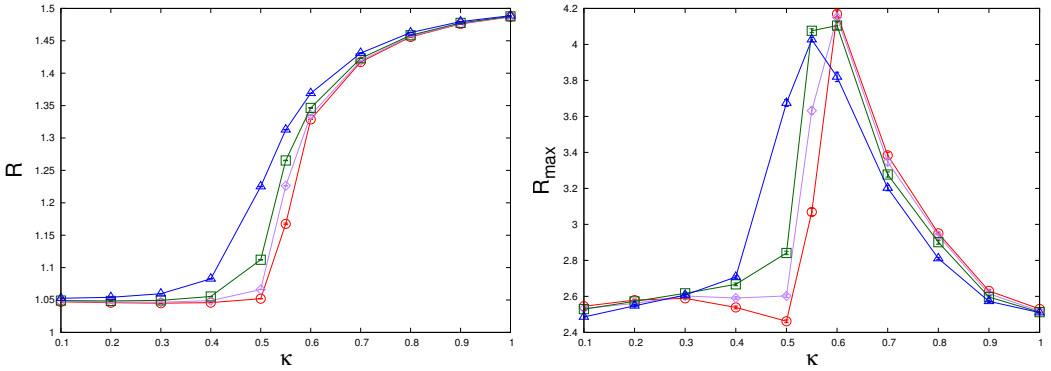

Figure 9. The κ-dependence of the mean value of the birth-death ratio with $\mu_{\rm iso} = 0, 5, 6$, and 7 where we take the configuration average. The top and bottom panels are the result of the averaged birth-death ratio (R) and the maximum birth-death ratio ($R_{\rm max}$), respectively. The open circle, diamond, square and triangle symbols are results with $\mu_{\rm iso} = 0, 5, 6$, and 7, respectively. Lines are just eye guides.

Finally, we show the ratio of birth and death times for each $(\kappa, \mu_{\rm iso})$ in Figure 10. The left and right panels show the averaged ratio (R) and the maximum ratio ($R_{\rm max}$), respectively. From the panels, we can image the behaviors of the averaged ratio and the maximum ratio in the whole $(\mu_{\rm iso}, \kappa)$ region. The behavior of the averaged ratio is well matched with the Polyakov loop, but we can see that the maximum ratio has more information about the system since the plateau structure, which may indicate the second-order transition, exists in the maximum ratio as mentioned before. Thus, the persistent homology has not only the information of the bulk properties of the system but also the spatial structure.

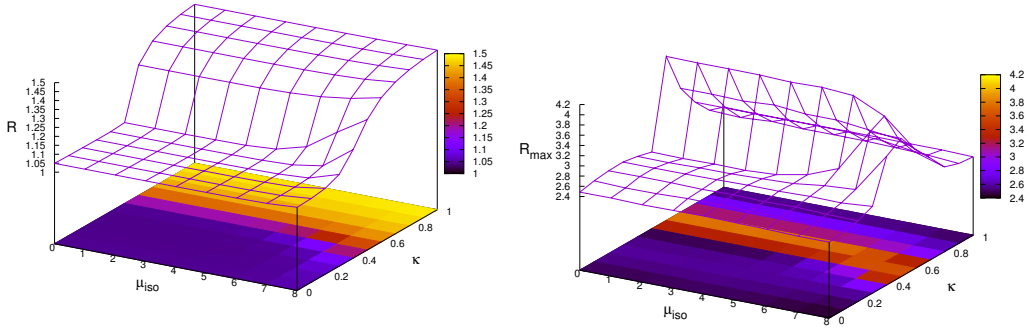

Figure 10. The mean value of the birth-death ratio on the $\mu_{\rm iso}$-κ plane where we take the configuration average. The left and right panels are the result of the averaged birth-death ratio R and the maximum $R_{\rm max}$, respectively. Statistical errors are very small, and thus, we do not show them here.

4. Summary

In this paper, we have investigated the phase structure of the three-dimensional three-state Potts model with finite isospin chemical potential ($\mu_{\rm iso}$); we call it the QCD-like Potts model. Since the Potts model with the external field has the sign problem, we sidestep the sign problem by using the isospin chemical potential. The spin configurations are then generated by using the QCD-like Potts model via the simple Metropolis algorithm, and the spatial structure of it is explored. Even if the isospin chemical potential leads to some differences in the QCD-like Potts model compared with the original one, we expect the

correct spin configuration to be mimicked at finite density via the QCD-like Potts model. Then, we performed a persistent homology analysis to investigate the spatial structure of the spin configuration.

It has been obtained that the averaged ratio of birth-and-death times is well matched with the behavior of the Polyakov loop, and thus, this quantity is only responsible for the bulk properties of the system. On the other hand, the maximum ratio of the birth-death ratio is expected to be responsible of the spatial structure in addition to the bulk properties of the system. We found that there may be no non-trivial spatial structure in the QCD-like Potts model at high and intermediate $\mu_{\rm iso}$; this can be seen from the behavior of the maximum ratio of birth-to-death times.

In the case of realistic QCD, we do not have a spin configuration, and thus, we need some further extension to use persistent homology. However, we can have the gauge configuration in QCD, and thus, a similar analysis can be possible; for example, we can classify each gauge field at each site from the viewpoint of the center symmetry structure of the Polyakov loop which has been employed in the investigation of the center clustering structure. Of course, gauge configurations are a more complicated quantities than the Potts spin, and thus, we need some more progresses for the analysis. We hope that this study sheds new light on exploring the phase structure of QCD at finite $\mu_{\rm R}$ from a topological point of view based on persistent homology.

Author Contributions: Conceptualization, K.K., T.H. and H.K.; methodology, K.K. and T.H.; analysis, K.K.; writing-original draft preparation, K.K.; writing-review and editing, K.K. and H.K. All authors have read and agreed to the published version of the manuscript.

Funding: This work is supported in part by the Grants-in-Aid for Scientific Research from JSPS (No. 18K03618, 19H01898, and 20K03974).

Institutional Review Board Statement: Not applicable.

Informed Consent Statement: Not applicable.

Data Availability Statement: Not applicable.

Conflicts of Interest: The authors declare no conflict of interest.

Appendix A. Problem of Complexification

One may wonder why we do not use complexification of dynamical variables in the present Potts model. This is because the complexification approach is quite powerful approach to sidestep the sign problem in QCD. In this section, first, we summarize the details of the complexification of dynamical variables in QCD and then discuss the problem that appears in the Potts model.

Appendix A.1. Complexification in QCD

It is well known that the $\mathcal{CK}$ symmetry imposed on the Dirac operator can sidestep the sign problem at least in the mean field level computation of the Nambu–Jona-Lasinio (NJL)-type QCD effective model, which includes the Polyakov loop dynamics [45,46]. In the following, all discussions are made with the Polyakov gauge fixing, $\partial_4 A_4 = 0$, and A_4 is then diagonalized by using the remaining spatial gauge degrees of freedom.

Without imposing the $\mathcal{CK}$ symmetry, the temporal gluon field (A^4) is given by

$$A^4(\mathbf{x}) = A_3^4(\mathbf{x})\lambda_3 + A_8^4(\mathbf{x})\lambda_8, \tag{A1}$$

and the Polyakov loop (Φ) then becomes

$$\Phi(\mathbf{x}) = \frac{1}{3}\left(e^{i\beta\phi_1(\mathbf{x})} + e^{i\beta\phi_2(\mathbf{x})} + e^{i\beta\phi_3(\mathbf{x})}\right), \tag{A2}$$

where λ_3 and λ_8 are diagonal components of the Gell–Man matrices, $\beta = 1/T$ is the inverse temperature and

$$\phi_1(\mathbf{x}) = A_3(\mathbf{x}) + \frac{A_8(\mathbf{x})}{\sqrt{3}}, \quad \phi_2(\mathbf{x}) = -A_3(\mathbf{x}) + \frac{A_8(\mathbf{x})}{\sqrt{3}}, \quad \phi_3(\mathbf{x}) = -\frac{2A_8(\mathbf{x})}{\sqrt{3}}. \tag{A3}$$

here, $A_3, A_8 \in \mathbb{R}$.

When we introduce the complexification of dynamical variables, the temporal component of the gluon field becomes the following:

$$A^4(\mathbf{x}) = [A_3^{4,\mathrm{R}}(\mathbf{x}) + iA_3^{4,\mathrm{I}}(\mathbf{x})]\lambda_3 + [A_8^{4,\mathrm{R}}(\mathbf{x}) + iA_8^{4,\mathrm{R}}(\mathbf{x})]\lambda_8, \tag{A4}$$

where $A_{3,8}^{\mathrm{R,I}} \in \mathbb{R}$. The $\mathcal{CK}$ symmetry imposed is corresponding to the setting with $A_3^{4,\mathrm{I}} = A_8^{4,\mathrm{R}} = 0$. This modification means that we replace the real A_8 with a pure imaginary one. This $\mathcal{CK}$ symmetric choice, Equation (A4) with $A_3^{8,\mathrm{I}} = 0$ and $A_8^{8,\mathrm{R}} = 0$, is the special case of the complexified dynamical variables approach. Of course, we can also complexify the third component of the gluon field A_3 if we want. This complexification has a similarity with the imaginary chemical potential [47,48].

It should be noted that the $\mathcal{CK}$ symmetry realization in the QCD effective model which includes the Polyakov-loop dynamics such as the Polyakov-loop-extended NJL (PNJL) model [49] is mathematically and numerically proven by using the Lefschetz thimble method [50] and the path optimization method [51], at least for the homogeneous solution. Although we do not know how the symmetry efficiently weakens the sign problem in realistic QCD including quantum fluctuations, we can expect that the symmetry weakens the sign problem.

Appendix A.2. Complexification in Potts Model

To introduce the complexification of dynamical variables into the Potts model, we encounter a serious problem since there are too many simplifications on the gauge field treatment in the Potts model.

The Polyakov loop in the Potts model with complexification of dynamical variables is defined as

$$\begin{aligned}\Phi(\mathbf{x}) &= \frac{1}{3}\left(e^{i\beta\tilde{\phi}_{1,\mathbf{x}}} + e^{i\beta\tilde{\phi}_{2,\mathbf{x}}} + e^{i\beta\tilde{\phi}_{3,\mathbf{x}}}\right),\\ \bar{\Phi}(\mathbf{x}) &= \frac{1}{3}\left(e^{-i\beta\tilde{\phi}_{1.\mathbf{x}}} + e^{-i\beta\tilde{\phi}_{2,\mathbf{x}}} + e^{-i\beta\tilde{\phi}_{3,\mathbf{x}}}\right),\end{aligned} \tag{A5}$$

where

$$\begin{aligned}\tilde{\phi}_{1,\mathbf{x}} &= A_{3,\mathbf{x}}^{4,\mathrm{R}} + iA_{3,\mathbf{x}}^{4,\mathrm{I}} + \frac{A_8^{4,\mathrm{R}}(\mathbf{x}) + iA_{8,\mathbf{x}}^{4,\mathrm{I}}}{\sqrt{3}},\\ \tilde{\phi}_{2,\mathbf{x}} &= -[A_{3,\mathbf{x}}^{4,\mathrm{R}} + iA_{3,\mathbf{x}}^{4,\mathrm{I}}] + \frac{A_{8,\mathbf{x}}^{4,\mathrm{R}} + iA_{8,\mathbf{x}}^{4,\mathrm{I}}}{\sqrt{3}},\\ \tilde{\phi}_{3,\mathbf{x}} &= -\frac{2[A_{8,\mathbf{x}}^{4,\mathrm{R}} + iA_{8,\mathbf{x}}^{4,\mathrm{I}}]}{\sqrt{3}},\end{aligned} \tag{A6}$$

here, the Potts model requires

$$\beta\frac{A_{8,\mathbf{x}}^{4,\mathrm{R}}}{\sqrt{3}} = \frac{2\pi k}{3}. \tag{A7}$$

To make the Potts energy real by using $A_3^{4,\mathrm{R}}$, $A_3^{4,\mathrm{I}}$, and $A_8^{4,\mathrm{I}}$, we can find one possible setting from the structure of the Dirac operator in QCD; the actual possible form is

$$A_3^{4,\mathrm{R}} = A_8^{4,\mathrm{R}}, \quad A_3^{4,\mathrm{I}} = -\frac{3}{2}\mu, \quad A_8^{4,\mathrm{I}} = \frac{\sqrt{3}}{2}\mu. \tag{A8}$$

With this setting, we can easily check that the Dirac operator is real. Then, Φ and $\bar{\Phi}$ become

$$\begin{aligned}\Phi(\mathbf{x}) &= \frac{e^{\mu/T}}{3}\left(e^{2\pi ik/3} + e^{-3\mu/T} + e^{4\pi ik/3}\right),\\ \bar{\Phi}(\mathbf{x}) &= \frac{e^{-\mu/T}}{3}\left(e^{4\pi ik/3} + e^{3\mu/T} + e^{2\pi ik/3}\right).\end{aligned} \tag{A9}$$

In this setting, all additional dynamical variables are fixed by using $\beta\mu$. Unfortunately, the above Polyakov loop and its conjugate take $\frac{1}{3} \leq \langle\Phi\rangle$ and do not match those behaviors in QCD even at $\mu = 0$. Since $A_{8,\mathbf{x}}^{4,\mathrm{R}}$ takes the specific values (A7) in the Potts model, and thus, we cannot suitably remove the sign problem via the complexification unlike the PNJL model: in the case of the PNJL model, we complexify A_8^4, but A_3^4 is kept as the real value.

References

1. De Forcrand, P. Simulating QCD at finite density. *PoS* **2009**, *LAT2009*, 010.
2. Nambu, Y.; Jona-Lasinio, G. Dynamical Model of Elementary Particles Based on an Analogy with Superconductivity. I. *Phys. Rev. D* **1961**, *122*, 345–358. [CrossRef]
3. Wu, F.Y. The potts model. *Rev. Mod. Phys.* **1982**, *54*, 235. [CrossRef]
4. De Forcrand, P.; Rindlisbacher, T. Spin models in complex magnetic fields: A hard sign problem. *EPJ Web Conf.* **2018**, *175*, 07026. [CrossRef]
5. Alexandru, A.; Bergner, G.; Schaich, D.; Wenger, U. Solution of the sign problem in the Potts model at fixed fermion number. *Phys. Rev. D* **2018**, *97*, 114503. [CrossRef]
6. Nishimura, H.; Ogilvie, M.C.; Pangeni, K. Complex spectrum of finite-density lattice QCD with static quarks at strong coupling. *Phys. Rev. D* **2016**, *93*, 094501. [CrossRef]
7. Akerlund, O.; de Forcrand, P.; Rindlisbacher, T. Oscillating propagators in heavy-dense QCD. *J. High Energy Phys.* **2016**, *10*, 055. [CrossRef]
8. Parisi, G.; Wu, Y.S. Perturbation Theory Without Gauge Fixing. *Sci. Sin.* **1981**, *24*, 483.
9. Parisi, G. On Complex Probabilities. *Phys. Lett.* **1983**, *B131*, 393–395. [CrossRef]
10. Cristoforetti, M.; Di Renzo, F.; Scorzato, L. New approach to the sign problem in quantum field theories: High density QCD on a Lefschetz thimble. *Phys. Rev. D* **2012**, *86*, 074506. [CrossRef]
11. Fujii, H.; Honda, D.; Kato, M.; Kikukawa, Y.; Komatsu, S.; Sano, T. Hybrid Monte Carlo on Lefschetz thimbles—A study of the residual sign problem. *J. High Energy Phys.* **2013**, *1310*, 147. [CrossRef]
12. Mori, Y.; Kashiwa, K.; Ohnishi, A. Toward solving the sign problem with path optimization method. *Phys. Rev. D* **2017**, *96*, 111501. [CrossRef]
13. Mori, Y.; Kashiwa, K.; Ohnishi, A. Application of a neural network to the sign problem via the path optimization method. *Prog. Theor. Exp. Phys.* **2018**, *2018*, 023B04. [CrossRef]
14. Hasenfratz, A.; Toussaint, D. Canonical ensembles and nonzero density quantum chromodynamics. *Nucl. Phys.* **1992**, *B371*, 539–549. [CrossRef]
15. Alexandru, A.; Faber, M.; Horvath, I.; Liu, K.F. Lattice QCD at finite density via a new canonical approach. *Phys. Rev. D* **2005**, *72*, 114513. [CrossRef]
16. Kratochvila, S.; de Forcrand, P. QCD at zero baryon density and the Polyakov loop paradox. *Phys. Rev. D* **2006**, *73*, 114512. [CrossRef]
17. de Forcrand, P.; Kratochvila, S. Finite density QCD with a canonical approach. *Nucl. Phys. Proc. Suppl.* **2006**, *153*, 62–67. [CrossRef]
18. Li, A.; Alexandru, A.; Liu, K.F.; Meng, X. Finite density phase transition of QCD with $N_f = 4$ and $N_f = 2$ using canonical ensemble method. *Phys. Rev. D* **2010**, *82*, 054502. [CrossRef]
19. Kashiwa, K.; Kouno, H. Anatomy of the dense QCD matter from canonical sectors. *Phys. Rev. D* **2021**, *103*, 114020. [CrossRef]
20. Kashiwa, K. Investigation of the Thermal QCD Matter from Canonical Sectors. *Symmetry* **2021**, *13*, 1273. [CrossRef]
21. Kashiwa, K.; Kouno, H. Multiplicity, probabilities, and canonical sectors for cold QCD matter. *Phys. Rev. D* **2022**, *105*, 054017. [CrossRef]
22. Hanada, M.; Yamamoto, N. Universality of Phases in QCD and QCD-like Theories. *J. High Energy Phys.* **2012**, *1202*, 138. [CrossRef]

23. Edelsbrunner, H.; Letscher, D.; Zomorodian, A. Topological persistence and simplification. In Proceedings of the 41st Annual Symposium on Foundations of Computer Science, Washington, DC, USA, 12–14 November 2000; pp. 454–463.
24. Zomorodian, A.; Carlsson, G. Computing persistent homology. *Discret. Comput. Geom.* **2005**, *33*, 249–274. [CrossRef]
25. Hirakida, T.; Kashiwa, K.; Sugano, J.; Takahashi, J.; Kouno, H.; Yahiro, M. Persistent homology analysis of deconfinement transition in effective Polyakov-line model. *Int. J. Mod. Phys. A* **2020**, *35*, 2050049. [CrossRef]
26. Gattringer, C. Coherent center domains in SU(3) gluodynamics and their percolation at T_c. *Phys. Lett. B* **2010**, *690*, 179–182. [CrossRef]
27. Borsanyi, S.; Danzer, J.; Fodor, Z.; Gattringer, C.; Schmidt, A. Coherent center domains from local Polyakov loops. *J. Phys. Conf. Ser.* **2011**, *312*, 012005. [CrossRef]
28. Endrodi, G.; Gattringer, C.; Schadler, H.P. Fractality and other properties of center domains at finite temperature: SU(3) lattice gauge theory. *Phys. Rev. D* **2014**, *89*, 054509. [CrossRef]
29. Donato, I.; Gori, M.; Pettini, M.; Petri, G.; De Nigris, S.; Franzosi, R.; Vaccarino, F. Persistent homology analysis of phase transitions. *Phys. Rev. E* **2016**, *93*, 052138. [CrossRef]
30. Olsthoorn, B.; Hellsvik, J.; Balatsky, A.V. Finding hidden order in spin models with persistent homology. *Phys. Rev. Res.* **2020**, *2*, 043308. [CrossRef]
31. Cole, A.; Loges, G.J.; Shiu, G. Quantitative and interpretable order parameters for phase transitions from persistent homology. *arXiv* **2020**, arXiv:2009.14231
32. Tran, Q.H.; Chen, M.; Hasegawa, Y. Topological persistence machine of phase transitions. *Phys. Rev. E* **2021**, *103*, 052127. [CrossRef] [PubMed]
33. Sale, N.; Giansiracusa, J.; Lucini, B. Quantitative analysis of phase transitions in two-dimensional XY models using persistent homology. *Phys. Rev. E* **2022**, *105*, 024121. [CrossRef] [PubMed]
34. Sale, N.; Lucini, B.; Giansiracusa, J. Probing center vortices and deconfinement in SU(2) lattice gauge theory with persistent homology. *arXiv* **2022**, arXiv:2207.13392.
35. Elbers, W.; van de Weygaert, R. Persistent topology of the reionization bubble network—I. Formalism and phenomenology. *Mon. Not. Roy. Astron. Soc.* **2019**, *486*, 1523–1538. [CrossRef]
36. Cole, A.; Shiu, G. Topological Data Analysis for the String Landscape. *J. High Energy Phys.* **2019**, *3*, 054. [CrossRef]
37. Alford, M.G.; Chandrasekharan, S.; Cox, J.; Wiese, U.J. Solution of the complex action problem in the Potts model for dense QCD. *Nucl. Phys.* **2001**, *B602*, 61–86. [CrossRef]
38. Kim, S.; de Forcrand, P.; Kratochvila, S.; Takaishi, T. The 3-state Potts model as a heavy quark finite density laboratory. *PoS* **2006**, *LAT2005*, 166.
39. Kashiwa, K.; Kouno, H. Information theoretical view of QCD effective model with heavy quarks. *Phys. Rev. D* **2021**, *103*, 014014. [CrossRef]
40. Lenz, J.; Pannullo, L.; Wagner, M.; Wellegehausen, B.; Wipf, A. Inhomogeneous phases in the Gross-Neveu model in 1+1 dimensions at finite number of flavors. *Phys. Rev. D* **2020**, *101*, 094512. [CrossRef]
41. Nakamura, T.; Hiraoka, Y.; Hirata, A.; Escolar, E.G.; Nishiura, Y. Persistent homology and many-body atomic structure for medium-range order in the glass. *Nanotechnology* **2015**, *26*, 304001. [CrossRef]
42. Hiraoka, Y.; Nakamura, T.; Hirata, A.; Escolar, E.G.; Matsue, K.; Nishiura, Y. Hierarchical structures of amorphous solids characterized by persistent homology. *Proc. Natl. Acad. Sci. USA* **2016**, *113*, 7035–7040. [CrossRef] [PubMed]
43. Obayashi, I.; Nakamura, T.; Hiraoka, Y. Persistent Homology Analysis for Materials Research and Persistent Homology Software: HomCloud. *J. Phys. Soc. Jpn.* **2022**, *91*, 091013. [CrossRef]
44. Matsumoto, M.; Nishimura, T. Mersenne twister: A 623-dimensionally equidistributed uniform pseudo-random number generator. *ACM Trans. Model. Comput. Simul. (TOMACS)* **1998**, *8*, 3–30. [CrossRef]
45. Nishimura, H.; Ogilvie, M.C.; Pangeni, K. Complex saddle points in QCD at finite temperature and density. *Phys. Rev. D* **2014**, *90*, 045039. [CrossRef]
46. Nishimura, H.; Ogilvie, M.C.; Pangeni, K. Complex Saddle Points and Disorder Lines in QCD at finite temperature and density. *Phys. Rev. D* **2015**, *91*, 054004. [CrossRef]
47. Roberge, A.; Weiss, N. Gauge Theories with Imaginary Chemical Potential and the Phases of QCD. *Nucl. Phys.* **1986**, *B275*, 734. [CrossRef]
48. Kashiwa, K. Imaginary Chemical Potential, NJL-Type Model and Confinement–Deconfinement Transition. *Symmetry* **2019**, *11*, 562. [CrossRef]
49. Fukushima, K. Chiral effective model with the Polyakov loop. *Phys. Lett.* **2004**, *B591*, 277–284. [CrossRef]
50. Tanizaki, Y.; Nishimura, H.; Kashiwa, K. Evading the sign problem in the mean-field approximation through Lefschetz-thimble path integral. *Phys. Rev. D* **2015**, *91*, 101701. [CrossRef]
51. Kashiwa, K.; Mori, Y.; Ohnishi, A. Controlling the model sign problem via the path optimization method: Monte Carlo approach to a QCD effective model with Polyakov loop. *Phys. Rev. D* **2019**, *99*, 014033. [CrossRef]